Congestus modes in circulating equilibria of the tropical atmosphere in a two-column model

Nuijens, Louise; Emanuel, Kerry

DOI
10.1002/qj.3385

Publication date
2018

Document Version
Accepted author manuscript

Published in
Quarterly Journal of the Royal Meteorological Society

Citation (APA)
Nuijens, L., & Emanuel, K. (2018). Congestus modes in circulating equilibria of the tropical atmosphere in a two-column model. *Quarterly Journal of the Royal Meteorological Society*, *144*(717), 2676-2692. https://doi.org/10.1002/qj.3385

ORIGINAL ARTICLE

Congestus modes in circulating equilibria of the tropical atmosphere in a two-column model

L. Nuijens[1]* | **K. Emanuel**[2]*

[1]Geoscience and Remote Sensing Department, Delft University of Technology

[2]Department of Earth, Atmosphere and Planetary Sciences, Massachusetts Institute of Technology

Correspondence
L. Nuijens, Geoscience and Remote Sensing Department, Delft University of Technology, Stevinweg 1, 2628 CN Delft, Netherlands
Email: louise.nuijens@tudelft.nl

Funding information

A two-column radiative-convective equilibrium (RCE) model

* Equally contributing authors.

is used to study the depth of convection that develops in the subsiding branch of a Walker-like overturning circulation. The model numerically solves for two-dimensional non-rotating hydrostatic flow, which is damped by momentum diffusion in the boundary layer and model interior, and by convective momentum transport. Convection, clouds and radiative transfer are parameterized, and the convection scheme does not include explicit freezing or melting.

While integrating the model towards local RCE, the level of neutral buoyancy (LNB) fluctuates between mid- and high-levels. Evaporation of detrained moisture at the LNB locally cools the environment, so that the final RCE state has a stable layer at mid-levels (550 hPa ≈ 50-100 hPa below 0°C), which is unrelated to melting of ice. Preferred detrainment at mid- and high-levels leaves the middle-to-upper troposphere relatively dry.

A circulation is introduced by incrementally lowering the SST in one column, which collapses convection: first to a congestus mode with tops near 550 hPa, below the dry layer created in RCE; then to congestus with tops near 650 hPa; and finally to shallow cumulus with tops near 850 hPa. Critical to stabilizing congestus near 650 hPa is large radiative cooling near moist cumulus tops under a dry upper atmosphere. This congestus mode is very sensitive, and only develops when horizontal temperature gradients created by evaporative and radiative cooling can persist against the work of gravity waves. This only happens in runs with ample momentum diffusion, which are those with convective momentum transport or large domains.

Compared to the shallow mode, the congestus mode produces a deep moist layer and more precipitation. This reduces radiative cooling in the cloud layer and enhances stability near cloud base, which weakens the circulation, and leads to less precipitation over the warm ocean.

KEYWORDS
congestus; Walker circulation; radiative-convective equilibrium; two-column model

1 | INTRODUCTION

Shallow convection has long been recognised as an important player in large-scale overturning circulations, in particular, in the Hadley circulation (Riehl *et al.*, 1951). The inflow branches of the Hadley circulation, the trades, are filled with shallow cumulus clouds, which increase the mixing of moist air away from the surface and of drier free tropospheric air towards the surface. Shallow convective mixing thus increases the surface enthalpy flux, which is important for coupling the atmosphere to the ocean, and which allows the trade-winds to accumulate heat and moisture as they travel equatorward.

When the European Center for Medium-range Weather Forecast (ECMWF) first introduced shallow convection in its model, increasing the ventilation of the boundary layer, the onset of deep convection was delayed, and the Intertropical Convergence Zone (ITCZ) narrowed (Tiedtke, 1989). By changing the rate of ventilation by shallow convection, Neggers *et al.* (2007) found a similar effect in an intermediate-complexity quasi-equilibrium tropical circulation model (QTCM).

Low-level cloudiness produced by shallow convection can also narrow regions with deep convection. Using a version of the QTCM to simulate a Walker-like overturning circulation, Bretherton and Sobel (2002a) and Peters and Bretherton (2005) showed that adding cloud-radiative cooling to the top of the boundary layer reduces the area occupied by deep convection. Cloud-resolving or rather cloud-permitting model (CRM) simulations of the aggregation of deep convection reveal a similar mechanism. Areas surrounding deep convection are relatively dry, and therefore have more low-level radiative cooling, which can be further enhanced by low-level clouds (Muller and Held, 2012; Wing and Emanuel, 2014; Hohenegger and Stevens, 2016). Large low-level cooling triggers a circulation that transports moist static energy into the deep convective region, leading to further aggregation of deep convection.

Changing the relative area of convecting and subsiding regions is critical for climate, because an increase in the area with subsidence and drying enhances the global emission of longwave radiation to space, which cools the Earth system (Pierrehumbert, 1995; Nilsson and Emanuel, 1999; Mauritsen and Stevens, 2015). Shallow convective mixing and low-level cloudiness might play an important role in setting those areas. Perhaps for different reasons, but demonstrating its effect on global climate, shallow convective mixing and low-level cloudiness also help explain why climate models diverge in their prediction of climate sensitivity (Sherwood *et al.*, 2014; Vial *et al.*, 2016).

In the context of these studies, the definition of shallow convection is not entirely clear. We interpret shallow convection as cumulus *humilis* or *mediocris* with tops up to 2 km. Indeed, these types of cumuli dominate the trades. But observations also show that episodes of shallow cumuli alternate with episodes in which deeper cumuli set the stage. With tops near 3 or 4 km and rain showers, these clouds are best marked as *congestus*. Episodes with more congestus last a few days to a week (Nuijens *et al.*, 2015), which suggests that they are tied to changes in the large-scale synoptic state, *e.g.*, atmospheric circulations. This leads us to wonder: what sets the depth of convection in the subsiding branch of a circulation? Is congestus a stable mode in circulating equilibria in the tropical atmosphere? And how does the presence of congestus change the character of the circulation?

Congestus as a third mode of tropical convection is well-known. Congestus tops are often observed near the freezing level (Johnson *et al.*, 1999; Jensen and Genio, 2006), although some fraction of diagnosed congestus are probably detrained cloud layers that accompany deep convection instead, or tropical cumuli that are on their way to the cumulonimbus stage (Luo *et al.*, 2009). Congestus is observed along with weakly stable layers. Such stable layers may arise from the melting of stratiform rain, which produces a local cool layer wedged between relatively warm layers (Mapes and Houze, 1995), and these may be maintained and reinforced through the combination of subsidence induced by gravity waves, and evaporative and radiative cooling of detrained condensate (Posselt *et al.*, 2008, 2011). The intrusion of dry layers from the mid latitudes may also create stable layers through their interaction with radiation

(Mapes and Zuidema, 1996; Yoneyama and Parsons, 1999; Pakula and Stephens, 2009).

CRM simulations of radiative-convective equilibrium and the TOGA COARE campaign reproduce the trimodality in tropical convection (Posselt *et al.*, 2008; Pakula and Stephens, 2009; Posselt *et al.*, 2011; Mechem and Oberthaler, 2013), but GCM's have difficulties reproducing such trimodality due to poor vertical resolution (Inness *et al.*, 2001) and the bimodal nature of convective parameterisations. In this paper we present numerical integrations with a far more idealised framework - a two-column radiative convective equilibrium model with parameterized convection - and show that it can produce congestus modes with tops near 3-4 km in the subsiding branch of circulating equilibria, without an explicit formulation of melting and freezing.

The two-column model we use numerically integrates the non-linear hydrostatic equations of motion for non-rotating flow in two side-by-side columns, and includes mechanical damping through momentum diffusion and surface drag. A linearised version of the model was first used by Nilsson and Emanuel (1999) (hereafter denoted by NE99), who studied the sensitivity of local RCE to changes in large-scale flow. NE99 forced the model with an annually averaged solar insolation at 30°, which, using an ocean mixed layer, gave a surface temperature of about 38°C in local RCE. NE99 demonstrated that with weak mechanical damping or small column length, local RCE becomes unstable due to a positive feedback between large-scale subsidence, advective drying and infrared cooling. The model developed a circulation with two possible equilibrium states. In the first state, the subsiding branch still supports deep convection, but the integrated heating vanishes due to the evaporation of precipitation. This circulation gave an SST of about 32°C in the subsiding branch, and ΔSSTs of about 0.6°C. In the other equilibrium state, convection in the subsiding branch vanished entirely, giving an SST of 30°C and ΔSSTs of 1.6°C. Along with a succession of other two-column model studies, NE99 thus exemplified the importance of subsiding dry areas in cooling climate (Pierrehumbert, 1995; Miller, 1997; Larson *et al.*, 1999; Nilsson and Emanuel, 1999; Bellon and Treut, 2003). But NE99 did not focus explicitly on the convective tops that were achieved, or their sensitivity to momentum diffusion and interactive radiation for a given SST difference. This is the goal of our present study, in which we start from a local RCE at 30°C, and force the circulation externally by increasing the SST difference between the columns.

We thus ignore the role of surface winds and the ocean at setting SSTs (Sun and Liu, 1996; Clement and Seager, 1999). Moreover, the two columns have equal length, ignoring the importance of the relative areas occupied by convection and subsidence. The two-box modelling framework thus greatly simplifies atmospheric dynamics, bypassing some of the complexity of GCMs, but the use of parameterized physics introduces uncertainties, as it does in GCMs. Despite its obvious limitations, we believe it is a useful tool for identifying key interactions that might be relevant for congestus in natural circulations, and which can be tested using a CRM or LES model.

We proceed as follows: In section 2 we describe the model physics and set up; in section 3 we discuss basic features of local RCE and explore the tendency of the model to produce trimodal convection; in section 4 and 5 we describe the circulating equilibria with congestus in the subsiding column, and discuss its sensitivity to radiation and mechanical damping. We summarize our work in section 6.

2 | THE MODEL AND EXPERIMENTAL SET UP

2.1 | Governing equations

The model is hydrostatic and based on the primitive equations for two-dimensional flow, which can be aligned in the zonal-height plane or meridional-height plane. The model has an ocean whose SST is prescribed in this study, and an atmosphere consisting of two vertical columns, which can exchange heat through an overturning circulation. In the current set up we focus on non-rotating zonal flow, which may be considered a mock-Walker circulation (Figure 1).

The model numerically solves the following equations for the temperature T, specific humidity q_v and the vorticity ($\eta = \nabla \times \vec{u}$):

$$\frac{\partial T}{\partial t} + u\frac{\partial T}{\partial x} + \omega\frac{\partial T}{\partial p} + \frac{\alpha\omega}{c_p} = \gamma\frac{\partial^2 T}{\partial x^2} + \frac{F_{\mathrm{SH}}}{c_p \Delta p} + Q_{\mathrm{R}} + F_{\mathrm{Q1}} \tag{1}$$

$$\frac{\partial q_v}{\partial t} + u\frac{\partial q_v}{\partial x} + \omega\frac{\partial q_v}{\partial p} = \gamma\frac{\partial^2 q_v}{\partial x^2} + \frac{F_{\mathrm{LH}}}{c_p \Delta p} + F_{\mathrm{Q2}} \tag{2}$$

$$\frac{\partial \eta}{\partial t} + u\frac{\partial \eta}{\partial x} - f\frac{\partial v}{\partial p} = \frac{\partial \alpha}{\partial x} + \gamma\frac{\partial^2 \eta}{\partial x^2} + \frac{\partial \nu(\partial \eta/\partial p)}{\partial p} + \frac{\partial F_c^u}{\partial p} \tag{3}$$

where the specific volume α is defined as:

$$\alpha = \frac{T\, R_d\, (1 - q_v + q_v/\epsilon)}{p} \tag{4}$$

Here, R_d is the gas constant for dry air, ϵ is the ratio of the molecular mass of water vapor to that of dry air, u is the zonal wind and ω is the vertical velocity in pressure coordinates. In Equations 1 and 2, c_p is the specific heat capacity of dry air, and γ represents the inverse of a damping time scale τ, corresponding to the domain size L (see below). F_{SH} and F_{LH} are the sensible and latent heat fluxes at the surface, which are applied to the first model layer Δp; Q_{R} is the net radiative heating tendency; and F_{Q1} and F_{Q2} are the heat source and moisture source/sink due to convection and condensation. In Equation 3, f is the Coriolis parameter, which is set to zero in this study; F_c^u is the tendency of the zonal wind due to convective momentum transport; and $\frac{\partial \nu(\partial \eta/\partial p)}{\partial p}$ represents the momentum flux divergence in the boundary layer. ν is a shear viscosity, which is a function of pressure as follows:

$$\nu = \begin{cases} 100\gamma\left(1 + \frac{p - p_s}{\Delta_{\mathrm{PBL}}}\right), & \text{for } p \geq p_s - \Delta_{\mathrm{PBL}} \\ 0, & \text{for } p < p_s - \Delta_{\mathrm{PBL}} \end{cases} \tag{5}$$

The flow is thus non-linear, and forced by a zonal gradient in specific volume (α), which is proportional to the virtual temperature. Enthalpy and moisture can be horizontally transported from one column to the other. The first terms on the right-hand side represent a simple Fickian damping of the flow in the model interior through diffusion at a time scale τ. There is no obvious choice for what τ should be, and here we use $\tau = 100$ days for a domain size $L = 3000$ km (Table 1). In the boundary layer, the flow is damped through momentum flux divergence (Equation 5), which linearly decreases from a maximum damping near the surface to zero damping above the boundary layer, whose depth equals Δ_{PBL}. Additionally, momentum in the model interior is damped through convective momentum transport (see also section 2.2). Friction near the surface is applied through a bulk formula for the momentum flux τ_s (see next section, Equation 9), and a free-slip condition is used at the model top.

The two columns are of equal size and 1500 km wide. Each atmospheric column has $N_z = 100$ number of vertical pressure levels in the control set-up (Table 1), with the model bottom at p =1000 hPa and the model top at p =5 hPa. The vertical resolution is 12.5 hPa up to p =100 hPa, above which the grid is refined from 5 hPa up to 2.5 hPa.

The equations are solved using a leapfrog scheme in time with an Asselin filter and homogeneous Neumann boundary conditions. The model integration is performed using a time step of 1 minute and continued until equilibrium is reached, usually after 300 days for RCE, and 100 days for the circulating equilibria (Table 1).

Parameters control set-up		
Domain, resolution and integration		
vertical levels	N_z = 100	
domain length	L = 3000	km
integration time	T = 300	days
time step	Δt = 60	s
Surface fluxes and damping		
sea surface temperature	SST = 30	°C
gust factor	**V** = 7	ms^{-1}
surface transfer coefficient	C_D = 0.0015	
damping time scale	τ = 100	days
PBL depth	Δ_{PBL} = 150	hPa
Radiation		
latitude	ϕ = 10	°
time step for radiation calls	Δt_r = 60	s
solar constant	S = 1382	Wm^{-2}
ocean albedo	A = 0.15	-
Microphysics		
warm-cloud autoconversion threshold	l_0 = 1.1	gkg^{-1}
fraction of rainshaft falling through clear-sky	σ = 0.15	

TABLE 1 Parameters used in the control set-up of the two-column model and which are varied in this study. Optimized values for all parameters used in the convection (microphysics) scheme can be found in (Emanuel and Zivkovic-Rothman, 1999).

2.2 | Parameterized physics

The model uses parameterized convection, radiation and clouds to calculate the tendencies of heat, moisture and vorticity. The convection scheme is that of Emanuel and Zivkovic-Rothman (1999), and is particularly attractive for our study because the scheme does not explicitly distinguish between shallow and deep convection, allowing the transition between shallow and deep convection to be determined entirely by the model physics. The scheme computes undiluted updrafts, unsaturated downdrafts (see the formulation of precipitation below), and upward and downward mass fluxes that are based on the buoyancy sorting hypothesis of Raymond and Blyth (1986), which assumes that mixing is episodic and inhomogeneous. The scheme uses a spectrum of mixtures, which each ascend or descend to their level of neutral buoyancy (LNB). The fraction of the total cloud base mass flux that will mix with the environment at any given level is a function of the vertical change in undiluted cloud buoyancy. An increase in buoyancy with height leads to entrainment, and a decrease in buoyancy with height leads to detrainment. The mass flux at cloud base is derived by assuming that the sub-cloud layer remains neutrally buoyant with respect to air just above the sub-cloud layer. In other words, the cloud base mass flux responds to the difference between the virtual temperature of a parcel lifted adiabatically from the sub-cloud layer and the virtual temperature of the environment just above the sub-cloud layer. Instead of a separate boundary layer scheme, this model uses dry adiabatic adjustment below cloud base.

The scheme also computes the influence of convection on the zonal and meridional wind (convective momentum transport, CMT). Momentum is transported by the buoyancy-sorted updrafts and downdrafts just like a passive scalar, and conserves the mass-integrated momentum. A tunable factor multiplies the wind tendency and controls the strength of the CMT.

The formulation of microphysics in the convection scheme assumes that stochastic coalescence is the main precipitation forming process in warm clouds, and that the Bergeron-Findeisen process leads to more efficient precipitation formation when ice is involved. All cloud condensate beyond a critical threshold l_0 is removed from the updraft, whereby l_0 is constant below 0°C and decreases linearly above 0°C. No specific melting or freezing processes are included. Precipitation, once formed, does not interact with cloud water. It is added to a single hydrostatic, unsaturated downdraft, which transports heat and water, and which evaporates precipitation depending on the ambient temperature and humidity. This requires a number of parameters to be specified, for instance, the area fraction of the precipitating downdraft, or the fraction of the precipitation that falls through unsaturated air. We here rely on values for these parameters that are fine-tuned to observations made during GATE and TOGA COARE (Emanuel and Zivkovic-Rothman, 1999). The specific parameters that are varied in this study are listed in Table 1.

The surface sensible and latent heat fluxes (F_{SH} and F_{LH}) and the momentum flux (τ_s) are parameterized using standard bulk aerodynamic formulae:

$$F_{SH} = \rho\, C_D\, |V_s|\, (\mathrm{SST} - T_1) \tag{6}$$

$$F_{LH} = \rho\, C_D\, |V_s|\, (q_{s(\mathrm{SST})} - q_1) \tag{7}$$

$$\tau_s = \rho\, C_D\, |V_s|\, V_1 \tag{8}$$

which uses a surface exchange coefficient C_D that is the same for heat. moisture and momentum, and the total absolute wind speed near the surface $|V_s|$. The latter is a function of the grid-box averaged surface wind speed, a gust factor, and a deep convective downdraft velocity scale (Emanuel and Zivkovic-Rothman, 1999).

Longwave radiation is calculated using the scheme of Morcrette (1991) and shortwave radiation is calculated following Fouquart and Bonnell (1980). The shortwave radiation that we use is an annual averaged value for 10° latitude, and is not time- or date-dependent. Temperature, water vapor and clouds fully interact with radiation at every time step, but can be held static if desired, which we do in sensitivity tests in section 5.1.

Lastly, cloudiness is calculated using the statistical scheme of Bony and Emanuel (2001), which uses a probability distribution function of the total water, whose variance and skewness are diagnosed from the amount of sub-grid scale condensed water produced by cumulus convection, as well as from large-scale super-saturation. The scheme was originally optimized for tropical cumulus convection over the Pacific warm pool, and has been noted to underestimate low-level cloudiness. Especially near the lifting condensation level or cloud base, values for cloud fraction are small. Therefore, we interpret low-level cloudiness and its radiative effect with some caution. Because studies have suggested that radiative effects from low cloud may play an important role in driving circulations (Bretherton and Sobel, 2002b; Muller and Held, 2012) this aspect certainly deserves more attention. But in this study we accept this shortcoming (along with others) and focus on understanding the mechanisms behind sensitivities to the physics, regardless of their imperfections.

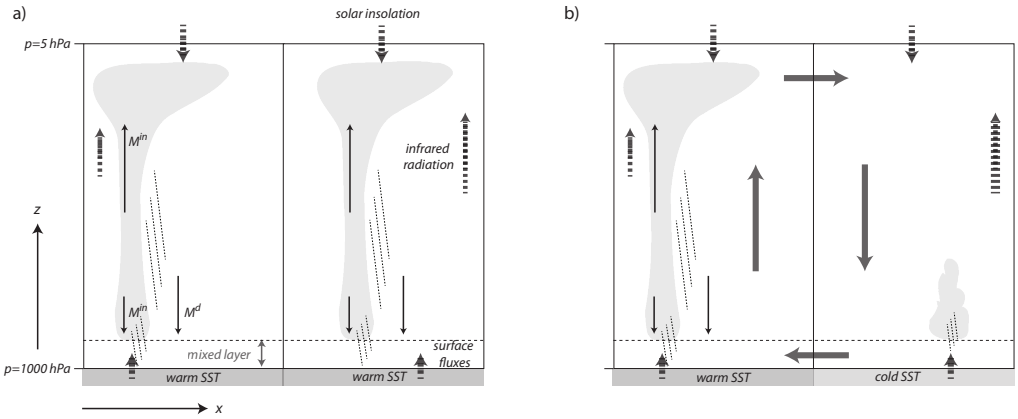

FIGURE 1 A schematic of the two-column model framework. a) The two columns supporting deep convection over warm SSTs, whereby each column is in local radiative-convective equilibrium. b) The SST of the rightmost column has been lowered, and convection over the colder ocean has collapsed. A circulating equilibrium between the two columns has been established, with mean ascent over the warm ocean and mean descent over the cold ocean.

3 | TRIMODAL CHARACTER OF CONVECTION IN RCE

For those less familiar with RCE and the two-column framework, we first summarize the main features of the local RCE state. In addition, we explore the tendency of the model to produce mid-level detrainment.

3.1 | Local RCE

The mean sounding of the TOGA COARE field campaign is used to initialise the model and calculate the radiative-convective equilibrium (RCE) state (Figure 1a). Technically, any sounding can be used, because the model physics control the final thermodynamic state. The model is forced with an SST of 30°C and the annual and daily averaged solar insolation at 10°. These and other control parameters are listed in Table 1.

For this set of control parameters, local RCE is a stable, but not necessarily steady solution. Stable oscillations in vertical velocity and radiative heating rates are present when clouds interact with radiation, and disappear using clear-sky radiation. Unlike NE99, we thus do not find that local RCE is unstable, with each column approaching the same equilibrium state. We believe this may be because NE99 ran their experiments at a much higher temperature, or because of the non-linearity of our model and use of prescribed SSTs, but we do not explore this further. We do note that convection in one column collapses when radiation is not called every time step, so that column-differences in (cloud-induced) heating rates can persist for long periods of time (Pauluis and Emanuel, 2004). Here we avoid this form of spontaneous aggregation by calling radiation every time step. The positive feedback between infrared cooling and subsidence via advective drying, responsible for the destablization of local RCE in NE99, is still evident in our model, because the collapse of convection with a surface cooling in one column occurs at smaller ΔSSTs when radiation is interactive (see also Figure 8 in section 5.1).

We run the model at three vertical resolutions (Δp =25 hPa, 12.5 hPa (control), and 6 hPa), which are plotted in Figure 2.

Convection in RCE has an upward mass flux that is positive up to 150 hPa (Figure 2a). This produces a convective

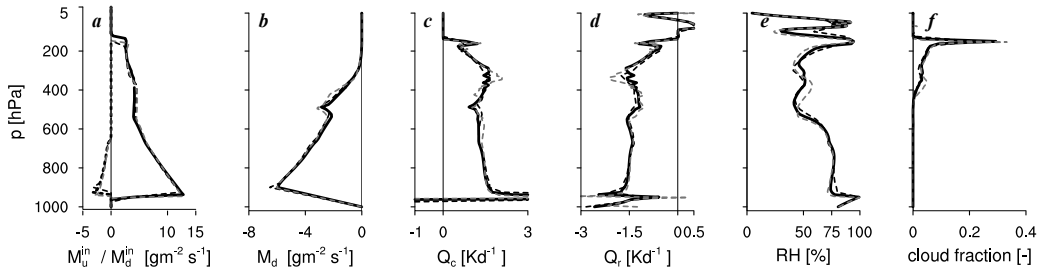

FIGURE 2 Profiles of the local radiative-convective equilibrium state of the columns at SST = 30°C for different vertical resolutions: Δp =12.5 hPa (control case - solid black line), Δp =25 hPa (dashed black line) and Δp =6 hPa (dashed grey line). The following variables are shown: a) the saturated upward mass flux M_u^{in} and downward mass flux M_d^{in}; b) the unsaturated precipitation-driven downward mass flux M_d; c) the convective heating rate Q_c; d) the radiative cooling rate Q_r; e) the relative humidity RH; and f) the cloud fraction.

heating that balances the radiative cooling rate of the atmosphere (Figures 2c and d). Precipitation produces unsaturated downward mass fluxes below 300 hPa (Figure 2b), and surface precipitation rates average to 5 mmd^{-1}. Cloudiness peaks in the upper atmosphere where the atmosphere is close to saturation, and is small at low-levels (Figures 2e and f).

The sensitivity of the model to vertical resolution is small, except for the sharpness of humidity gradients, which slightly increases with resolution. The humidity profile reveals a relatively moist lower atmosphere, whereas levels above 600 hPa are relatively dry. As dry levels are hypothesized to be important for congestus, and we find congestus in the subsiding branches of the circulating equilibria that develop from local RCE, the next section describes a set of idealized experiments to explore what processes influence this particular structure in RCE.

3.2 | Mid-level detrainment in RCE

The 0°C level in RCE is located at about 500 hPa, which is where small peaks in the unsaturated downward mass flux and convective heating are found (Figures 2b and c), and which is about 50 hPa above a large relative humidity gradient (Figures 2d). Although the convection scheme does not have explicit freezing or melting processes, a number of physical parameters change value across 0°C. Among these are the liquid water threshold for rain formation, l_0 (section 2.2), the evaporation rate, the fall speed of precipitation (Emanuel and Zivkovic-Rothman, 1999), and the saturation vapor pressure. To remove the influence of these parameters on the humidity and stability structure in RCE we carry out a number of idealised experiments in which these parameters are vertically uniform. In addition, we remove condensate from the parcel updraft immediately, by setting the condensate-to-rain threshold l_0 to 0. This implies that condensate does not play a role in setting the mixture's detrainment levels. And finally, we do not let any precipitation evaporate on its way to the surface. We also use clear-sky radiation to make sure that changes in radiative cooling caused by thermodynamics are not overshadowed by those from excessive cloudiness. The RCE state that develops is plotted (with a long dashed black line) alongside the control RCE state (with a solid black line) in the top panels a - f in Figure 3.

With uniform microphysical parameters, the signature of the 0°C level in the convective heating and radiative cooling profiles disappears (Figure 3b and c). Evidently, without evaporation of precipitation the lower atmosphere is much drier (Figure 3d). Because detrainment is the only process that can moisten the atmosphere, this experiment thus reveals a preference of convection to detrain moisture near 650-550 hPa, rather than in the lower or upper atmosphere.

We also see a strong increase in stability near 550 hPa (Figure 3e), which could develop from the interaction of

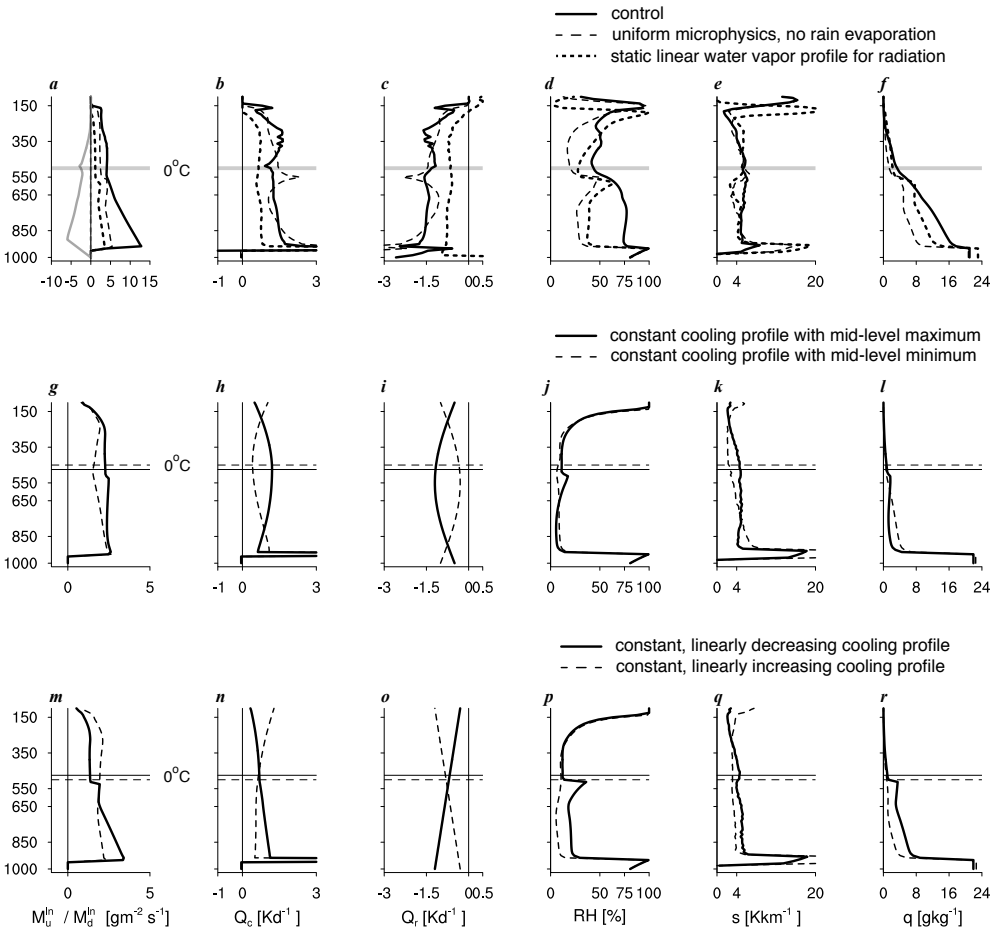

FIGURE 3 Profiles of the RCE state of the columns at SST = 30°C (*e.g.*, Figure 1a.) for a set of runs with increasing simplifications (see text for details) including using clear-sky radiation calculations. In the top row we show the control run (solid line), a run with uniform (micro)physical parameters and no evaporation of precipitation (long dashed line), and a run in which radiation is constant and calculated using the initial TOGA COARE temperature sounding and a linearly decreasing water vapor profile (short dashed line). The 0°C level of all three runs is near 500 hPa. In the middle and bottom rows we show runs with a constant idealised radiative cooling profile, which either has a maximum in cooling at mid-levels (solid line) or a minimum (dashed line), with slight differences in their respective 0°C levels. The same for the bottom row, but for a radiative cooling profile which maximizes near the surface and linearly decreases with height (solid line) or the reversed (dashed line). Variables plotted are: a) the saturated upward mass flux M_u^{in} and downward mass flux M_d^{in}, b) the convective heating rate Q_c, c) the radiative cooling rate Q_r, d) the relative humidity, e) the static stability s and f) the specific humidity q.

radiation with the relatively dry layer overhead (Mapes and Zuidema, 1996; Pakula and Stephens, 2009). Dry layers in the atmosphere are common and have indeed been observed along with stable layers near their base. Stable layers can also be produced by the melting of stratiform precipitation.

However, moisture-radiation interactions are not critical for mid-level entrainment here, because the stable layers also develops without it. In an additional idealisation we use for radiation calculations the initial TOGA COARE temperature profile, which does not have pronounced stable layers, and a monotonically decreasing water vapor profile that is constant in time (dotted line in Figure 3a-f). This removes the peak in radiative cooling (Figure 3c), but mid-level detrainment and enhanced stability remain. Thus, it appears that mid-level detrainment is inherent to the convection scheme.

The convection scheme is based on episodic mixing: it assumes a spectrum of mixtures at each level between cloud base and the level of neutral buoyancy (LNB) of an initial undiluted parcel. These mixtures each ascend or descend to their new LNB, where they detrain. If a mixture contains cloudy air, it may become negatively buoyant upon detraining and mixing with the environment, undergoing yet another ascent or descent. To deal with the impracticality of formulating multiple mixing episodes, the convection scheme insists that mixed air detrains at a level at which further mixing with the environment results in neutral buoyancy. To do so, the scheme lets mixtures detrain at a level at which their liquid water potential temperature, rather than their potential temperature, equals that of the environment Emanuel (1991).

The behaviour of mixing is illustrated in Figure 4, which show profiles of detrained and entrained mass fluxes at hour 0.00 on day 2, 10 and 30, along with profiles of the liquid water static energy h_w of the environment (solid line) and of the undiluted parcel (dashed line). Note that if the parcel would not precipitate, its liquid water static energy would be conserved (constant with height). Because all condensate is precipitated out immediately, the parcel's (liquid water) static energy increases with height above cloud base. Figure 4a shows that detrainment at the selected times maximizes near cloud base (950-850 hPa), mid-levels (600-500 hPa), and the tropopause (200-100 hPa). The LNB of the undiluted parcel fluctuates rapidly in time and is often just below 550 hPa, such as on hour 0.00 on day 10 and 30. On day 30, for instance, air detraining at low levels is coming down in downdrafts that have resulted from mixing between 950-700 hPa (Figure 4a, b). Detrainment is absent between 700-600 hPa, which is where the parcel's $h_{w,p}$ is approximately equal to that of the environment. At those levels entrainment takes place (Figure 4c), and the mixtures are detrained again near their LNB.

When mixtures detrain at a level at which their liquid water potential temperature equals that of the environment, the temperature of the environment cannot be changed. The exception is the LNB of the undiluted parcel, where $h_w \neq h_{w,p}$. Here, convective tops can cool the environment, which is evident in the profile of h_w on day 30, as well as in the enhanced stability near 550 we already saw in Figure 3e. As convective tops are cooling the environment, lapse rates at mid-levels can become superadiabatic. At subsequent time steps, undiluted parcels can therefore easily travel all the way up to the tropopause. Detrained air near the tropopause comes mostly from entrained air below, and between mid- and high-levels very little detrainment takes place (Figure 4a, d). As a result, the layer above 550 hPa remains relatively dry.

Apparently, as long as the environment is relatively stable to convection at mid- and high-levels, and the parcel's static energy is similar to that of the environment below the LNB, all the detrainment takes place at the LNB. If the environment at high-levels is destabilised sufficiently, and the parcel's static energy exceeds that of the environment, detrainment is more uniform. This requires a certain structure in the radiative cooling profile, which the middle and bottom rows of Figure 3 illustrate. Here, we have further idealized the uniform microphysics run by prescribing a constant radiative cooling profile that either minimises or maximizes at mid-levels (middle row), or linearly increases or decreases with height (bottom row). The mixing behaviour and (liquid water) static energy profiles of the runs with

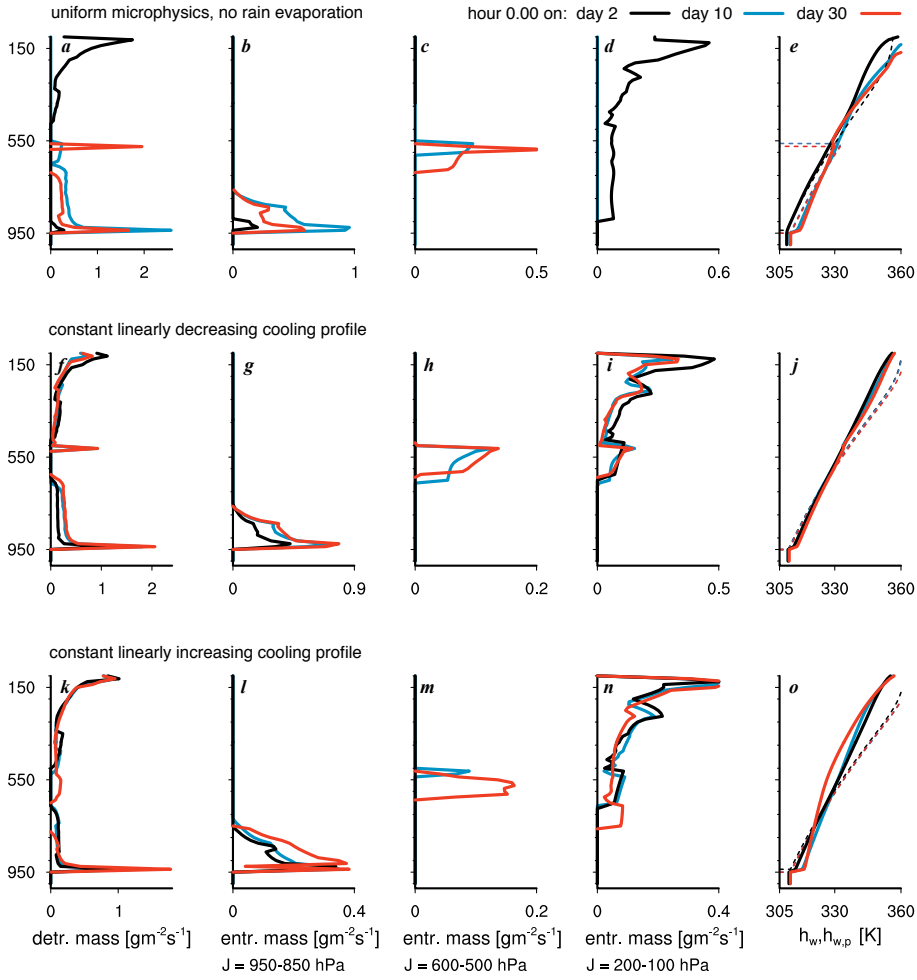

FIGURE 4 Instantaneous profiles of the detrained and entrained mass flux of mixtures taken on hour 0.00 on day 2, 10 and 30 for the runs with uniform microphysics in Figure 3 (top row), and additionally, with a constant radiation profile, which decreases with height (middle row) or increases with height (bottom row), as in Figure 3m-r. Plotted are: a) the distribution of net detrained mass at each level, b) the distribution of entrained mass that is detrained at levels J = 950-850 hPa, c) same as in b) but for levels J = 600-500 hPa, d) same as in b) but for levels J = 200-100 hPa, e) the liquid water static energy of the environment h_w (solid line) and of the parcel (dashed line).

a linear radiative cooling profile are also shown in Figure 4. Only the runs where radiative cooling decreases above mid-levels produce a peak in detrainment at mid-levels (Figure 3j and p, solid lines). When radiative cooling is constant with height (not shown) or increases with height above mid-levels (Figure 3i and o, dashed lines) a peak in mid-level detrainment disappears (Figure 4k, *e.g.*, red line).

These experiments, as idealised as they are, illustrate the complexity of RCE, and suggest that besides interactive radiation and the evaporation and melting of precipitation, convection may favour mid-level detrainment as long as high levels experience less destabilization than low levels.

In the following section, we show how a circulation collapses convection in the subsiding column, and how sensitive the presence of congestus is to radiation and mechanical damping of the flow. How the two-column model can evolve from a state of local RCE to a circulating equilibrium has been described by NE99. They emphasised the positive feedback between the circulation, which develops when convection in one column (temporally) ceases and leaves a net cooling, and the resulting drying from large-scale subsidence, which further enhances the cooling due to increased emission of infrared radiation. In our study, the presence of this feedback is less critical, because we externally force the circulation by imposing a SST difference, and we shall see that this will lead to the collapse of convection and the development of a circulation even when radiation is held constant.

4 | A THERMALLY-FORCED CIRCULATION

Using the RCE state of the control case, a circulation is forced by lowering the SST in one of the columns by increments of 0.25°C. Over the colder ocean, convection collapses, and the absence of deep convection cools the upper troposphere. This creates a heating contrast with the other column where convection is still deep, and therefore, high-level winds will blow from the warm to the cold column, and sinking motion develops over the cold ocean (Figure 1b). A circulating equilibrium develops within 100 days, usually already after 30 days. RCE has then been replaced by a balance between (shallow) convective heating, radiative cooling and subsidence warming over the cold ocean, and (deep) convective heating, radiative cooling and adiabatic cooling over the warm ocean.

4.1 | Trimodal character of convection over the cold ocean

The thermodynamic profiles and convection that develop as a function of ΔSST for the control set-up are shown in Figure 5. Convection over the cold ocean collapses with ΔSST, but the collapse is step-wise as follows. For small SST differences (ΔSST<0.5°C) convection over the cold ocean remains deep with stable convective tops near 150 hPa (brown-hued profiles in Figure 5g), but much less mass flux penetrates to 150 hPa, as compared to the deep convection over the warm ocean (Figure 5a). When ΔSST = 1°C (green-hued profiles) convection collapses further to a congestus mode, first to about 550 hPa and then to 650 hPa. The 0°C level of these runs is located at about 500 hPa, thus, above the congestus tops. When ΔSST>1.5°C (blue-hued profiles) convection collapses to a shallow mode with tops near 875 hPa. We used SST increments even smaller than 0.25°C (not shown) to confirm that the collapse of convective tops is indeed step-wise, and the jumps are much larger than the model's vertical grid spacing.

The convective tops, defined as the maximum level of positive convective mass flux, are also plotted in Figure 6a as a function of ΔSST, for three vertical resolutions:Δp =25 hPa (black dashed line), Δp= 12.5 hPa (control, solid black line), and Δp= 6 hPa (black dot-dashed line).The colours correspond to the colours of the profiles in Figure 5. The squares denote the mean convective top over the last 30 days of model integration, and vertical bars through the squares denote the minimum to maximum convective top during those 30 days. The latter gives an indication of how stable the modes

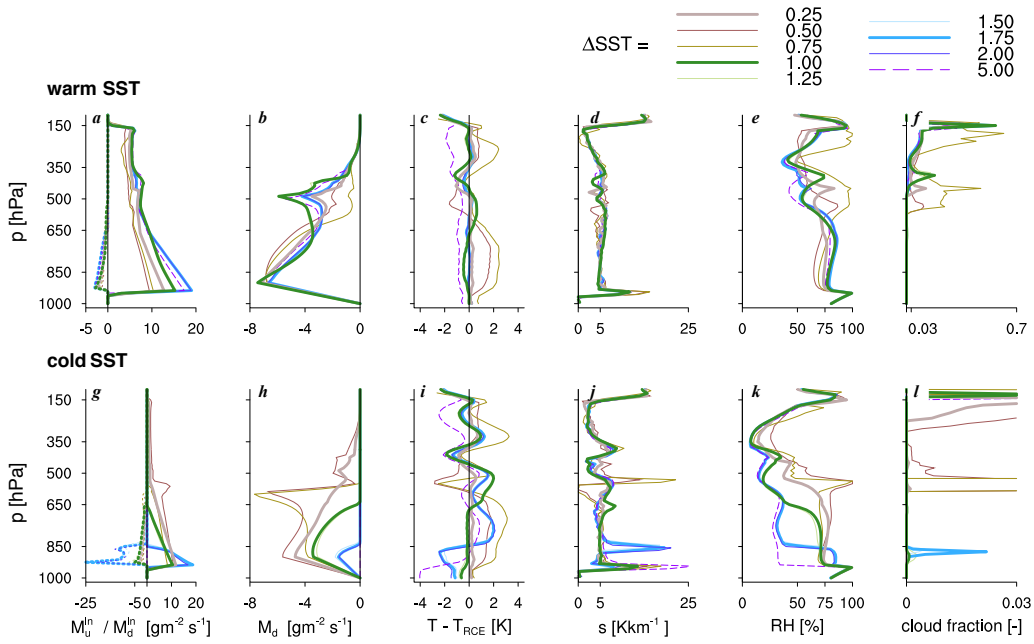

FIGURE 5 The mass flux, thermodynamic and cloud vertical structure in the warm SST (top panels) and cold SST column (bottom panels) as a function of ΔSST. Plotted are: a,g) the saturated (in-cloud) upward mass flux (M_u^{in}) and downward mass flux (M_d^{in}); b,h) the unsaturated out-of-cloud downward mass flux (M_d); c,i) the temperature minus the initial temperature in the RCE state; d,j) the static stability S; e,k) the relative humidity RH; and f,l) the cloud fraction.

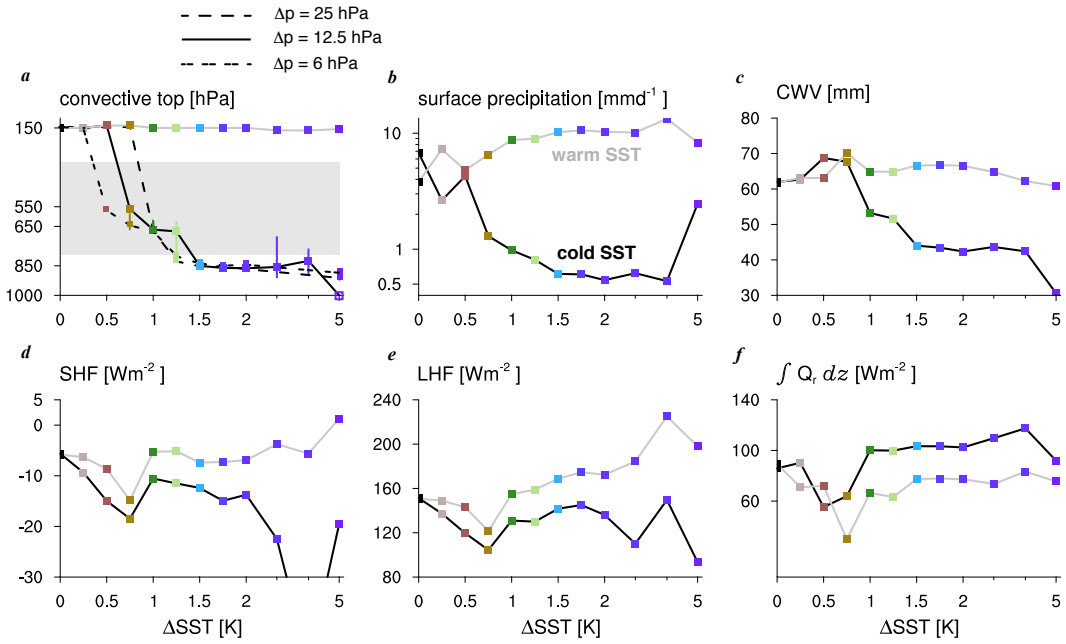

FIGURE 6 a) Convective tops as a function of the SST gradient (ΔSST), with black lines for the cold SST column (Δp = 12.5 hPa), and grey lines for the warm SST column. Additional black lines indicate different vertical resolutions (Δp = 25 hPa, black dashed line, and Δp = 6 hPa, black dot-dashed line). Convective tops are defined as the maximum level of positive in-cloud mass flux. When no mass flux is present, the convective top is put at 1000 hPa. Unstable tops are denoted with a vertical bar, which stretches from the minimum and maximum top that is attained in the last 30 days of model integration. The grey shading indicates tops belonging to congestus (from 2 - 8 km). Other variables shown are: b) the surface precipitation rate, c) the column water vapor, d) the sensible heat flux, e) the latent heat flux and f) the radiative cooling rate integrated from the surface up to 500 hPa.

are, and reveals that convective tops for ΔSST = 0.75 - 1.25°C oscillate between shallow and congestus modes. At all resolutions a congestus mode appears, but at a lower resolution convection collapses at larger ΔSST, passing through only one congestus mode, and at a higher resolution convection collapses already at ΔSST = 0.5°C, but goes through a few congestus modes first. At ΔSST > 2°C, convection becomes very shallow, and approaches what may be thought of as a stratocumulus regime. But in the absence of convection, the model physics (*e.g.*, the absence of a separate boundary layer scheme) are no longer appropriate, and the results should not be over-interpreted.

Alternatively, we could have raised the SST from a colder RCE state, whose atmosphere is overall drier. The circulations that develop are sensitive to this initial moisture structure, and there is some hysteresis between runs that start out at different SSTs. However, this hysteresis does not change the character of the circulation or the appearance of congestus, and here we only show results of runs starting from a warm RCE state. We also note that for some parameter settings non-linear behaviour in convective tops at low ΔSSTs is observed (*e.g*, Figure 6b). These are caused by a weak oscillatory circulation between the columns, when large cloud fractions are produced at mid-levels, which significantly lower radiative cooling in the lower troposphere and can reverse the circulation.

The two-column model is thus able to develop both shallow and congestus modes in the subsiding branch of the circulation. Why the experiments by NE99 develop either deep or no convection at all, for similar SST differences, might

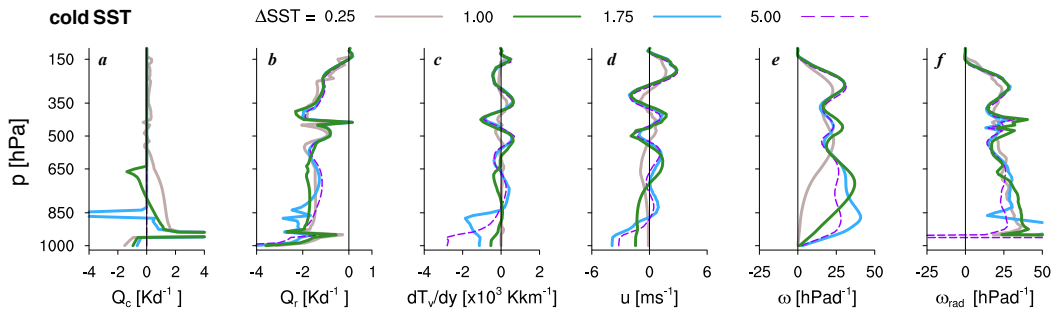

FIGURE 7 Profiles of the structure of the circulation and the convective and radiative heating tendencies over the cold SST column. Plotted are: a) the heating tendencies due to convection Q_c; b) the radiative cooling profile Q_r; c) the virtual temperature (buoyancy) gradient between the two columns dT_v/dy; d) the horizontal velocity u at the column boundary; e) the vertical velocity over the cold ocean ω^{cold}; f) the radiative vertical velocity $\omega_{\text{rad}}^{\text{cold}}$ (see text for further explanation).

be because of their use of a mixed-layer ocean. The greater coupling of atmosphere and ocean can reduce variability in convective tops, because stronger surface winds and larger infrared emission to space with a strengthening circulation reduce the SST and the surface evaporation. NE99 also use clear-sky conditions in their radiation calculations. We do not further explore these differences here.

The model version of NE99 also does not include an explicit boundary layer with momentum diffusion as in Equation 5, and it does not include convective momentum transport. Their model develops a very thin mechanical boundary layer (≈ 50 hPa), which becomes decoupled from the free troposphere and separated by an inversion, once the flow gets very strong. These runs do not even sustain shallow convection. We will show that when we increase the mechanical damping, our model version also develops only deep and shallow convection, or shallow convection ceases completely.

Before we discuss the sensitivity of the congestus modes to model physics, we next describe the different character of the circulating equilibria that develop in the presence of these modes.

4.2 | Circulating equilibria with convective heating over the cold ocean

In the circulating equilibria of NE99 that no longer support any convection, the radiative cooling over the cold ocean is balanced by vertical advective warming, and the strength of the circulation is a strong function of that radiative cooling, especially in a nearly inviscid atmosphere. In our experiments, the radiative vertical velocity ($\omega_{\text{rad}}^{\text{cold}}$), which is the vertical velocity required to balance the radiative cooling Q_r (Figure 7b) divided by the profile of stability (Figures 5d,j) also closely follows that of ω^{cold} above convective tops (Figure 7f). (Note that because we only use two columns, mass conservation dictates that mean ascent in the warm column equals descent over the cold ocean: $\omega^{\text{warm}} = -\omega^{\text{cold}}$. Therefore, we do not show vertical velocity profiles over the warm column.)

But below convective tops the convective heating (or cooling) is large enough to either counteract or reinforce (radiative) cooling, and thus becomes a significant term in explaining the profile of low-level winds. When deep convection over the cold ocean has collapsed, the heating contrast maximizes near the tops of the cold-side convection, where radiative and evaporative cooling peak. Horizontal flows from the warm to the cold column are strongest near those convective tops (Figure 7c), and also subsidence peaks here (Figure 7d). The horizontal wind reverses twice more above 650 hPa, which gives three overturning cells. This illustrates that overturning circulations are not necessarily deep

overturning circulations. Shallow return flows and mid-level inflows on the scale of the Hadley / Walker circulation are observed in the real atmosphere, in different ocean basins and in different seasons (Zhang *et al.*, 2008). Shallow return flows are also reproduced in a mesoscale numerical model with an equatorial channel configuration (Nolan *et al.*, 2010), and three overturning cells have been emphasised in CRM simulations of RCE (Posselt *et al.*, 2008).

The congestus mode is accompanied with a more humid layer between 800-650 hPa, which reduces radiative cooling of layers underneath. Low-level divergence and surface winds are therefore considerably weaker compared to the shallow mode. In the experiment with ΔSST = 5°C (dashed purple line in Figures 5 and 7), convection has ceased completely, which results in a very dry free troposphere and lack of cloudiness (Figures 5 h and i). Both reduce the radiative cooling between 950 and 650 hPa (Figure 7b), and hence the surface winds (Figure 7d) and low-level subsidence (Figure 7e) are even weaker than in the run with ΔSST = 1.75 °C. A simple conceptual model derived in Emanuel (2007) explains how the strength of the circulation in a two-box atmosphere becomes ultimately controlled by the rate of radiative cooling over the cold ocean, which has to be balanced by subsidence, in the absence of convective heating. However, in real atmospheres, the relative size of the subsidence area can vary, which allows for additional increases in circulation strength. Nevertheless, a number of studies show that radiative heating from clouds or the humidity gradient at the boundary layer top have as large an influence on circulation strength as SSTs *e.g.*, Bretherton and Sobel (2002a); Peters and Bretherton (2005) and Naumann *et al.* (2017). This challenges a widely accepted class of theory (Lindzen-Nigam), in which winds are determined by SST gradients, neglecting pressure gradients at the top of the boundary layer.

Convection over the warm ocean remains deep as ΔSST changes (Figures 5a and 6a). But the upward mass flux at cloud base approximately doubles from ΔSST = 0.25 °C to 1.75 °C, as the stability near cloud base decreases with stronger radiative cooling there (remember that the scheme adjusts the cloud-base mass flux in response to the difference between the density temperature of a parcel lifted from the sub-cloud layer and that of the environment near the lifting condensation level). This can be seen from the temperature anomaly profiles over the cold ocean (Figure 5i, whereby the anomalies are taken with respect to the same initial temperature profile in RCE), and is also true over the warm ocean, although smaller there (Figure 5c). The larger mass flux and enhanced drying of the sub-cloud layer (along with stronger surface winds) lead to larger surface evaporation and larger precipitation rates over the warm ocean (Figures 6b and e). Consistent with studies cited in the introduction, more low-level radiative cooling, produced by more low-level cloud amount or moist boundary layers underneath dry free troposphere, strengthens the circulation, which increases surface precipitation from deep convection. Hence, when the congestus mode develops, which has significantly less low-level radiative cooling, less deep convective precipitation is present over the warm ocean.

5 | SENSITIVITY TO MODEL PHYSICS

5.1 | Stabilizing roles of radiation

Dry and stable layers have been hypothesized as important for halting congestus tops. Although the model's RCE state develops stable layers in the absence of moisture-radiation interactions, we may still ask how radiation influences the development of congestus in the subsiding branch of the circulation.

In fact, we find that a stable congestus mode only develops with moisture-radiation interactions. Figure 8a shows a number of sensitivity tests. The control runs with interactive radiation are denoted with a solid black line. Experiments whereby only temperature interacts with radiation are shown in dashed black. Here, water vapor and cloud profiles from the RCE state are used for radiation calculations (denoted as static water vapor and clouds). The grey dashed line corresponds to runs with a constant radiative cooling, whose profile is that of the final RCE state. The difference

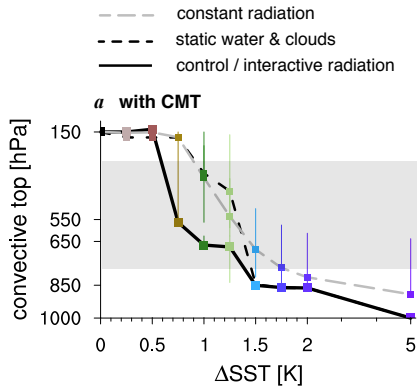

FIGURE 8 Convective tops over the cold ocean as a function of ΔSST, as in Figure 6a). The two panels show the fully interactive radiation run (control case) with a solid black line, along with runs using fixed radiation (in dashed grey), whereby fixed means that the radiative cooling profile from the RCE state is used at every time step; and runs using static water vapor and clouds, which means that the radiation scheme sees the water vapor and cloud profile from the RCE state, and only the temperature profile is interactive (in short dashed black).

between the runs with constant radiation and with static water vapor is just the interaction of radiation with the temperature profile. Apparently, this interaction stabilizes the shallow modes for ΔSST $\geq$ 1.5 K by strongly reducing the emission of infrared radiation underneath the inversion that caps shallow cumulus tops (not shown).

But to stabilize the congestus mode, the interaction of the moisture profile with radiation is also necessary. The time-pressure plots in Figure 9 reveal the thirty-day evolution of convection as it collapses to a congestus mode, either with or without moisture-radiation interactions. The panels show the convective mass flux, relative humidity, static stability, radiative cooling and advective drying over the cold ocean, after applying a ΔSST =of 1.25°C. Initially, convection in both runs collapses to about 650 hPa. This level is the LNB, which demonstrates how important the SST and initial parcel buoyancy are at setting convective tops. This level also coincides with the base of the weakly stable layer established in RCE (Figure 9c)), which suggests that deep convection may influence the depth of shallower convection by help setting the humidity structure and stability of the atmosphere.

In the following days, convection in the experiments with static water vapor slowly deepens, despite the presence of the deep dry layer above 600 hPa (Figure 9b). In contrast, convection in the interactive radiation runs collapses again and again until an equilibrium is reached with convective tops near 650 hPa. The difference between interactive radiation and static water vapor is that interactive radiation can increase the stability near the tops of detraining cumuli, and at the base of dry layers (Figure 9c). Through the circulation, changes in radiative cooling also maximise subsidence and subsidence drying near cumulus tops (Figure 7e,f and 9e).

5.2 | Sensitivity to mechanical damping

Congestus is not only sensitive to radiation. Besides thermal processes, the viscosity of the flow plays an important role in setting the strength of the circulation and the tops of convection. As we will show, the ability of the model to develop a congestus mode critically depends on the presence of sufficient momentum diffusion.

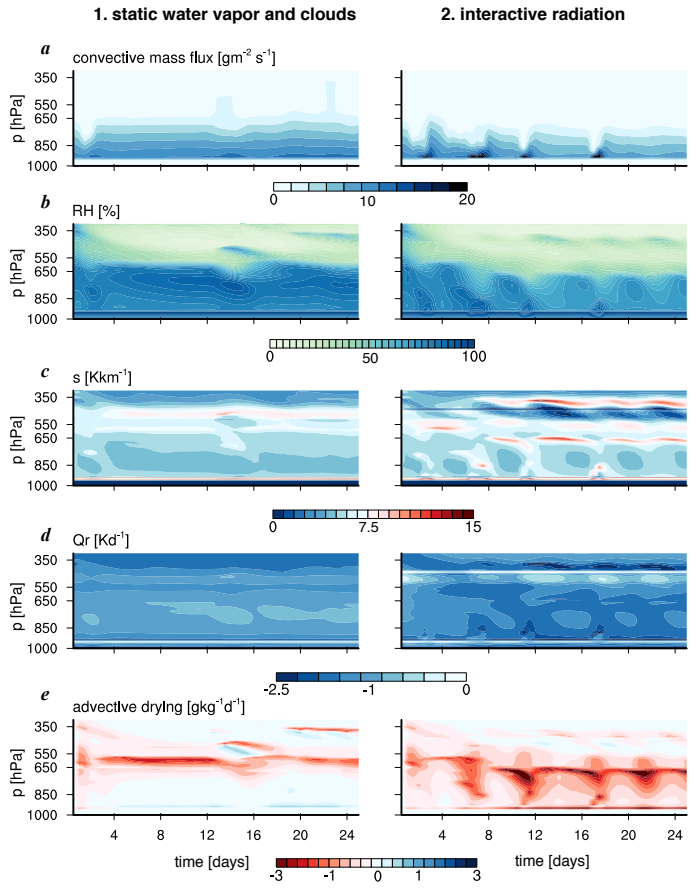

FIGURE 9 The evolution of the cold column during the first 30 days after lowering the SST by 1.25°C from an RCE state. Contour plots are shown for the run with static water vapor and clouds for radiation, and with interactive radiation (see also Figure 8). Variables plotted are a) the convective mass flux, b) relative humidity, c) the static stability, d) radiative cooling and e) drying from vertical advection.

5.2.1 | Momentum diffusion in model interior

The control experiments we have described so far are run using a domain length of 3000 km. The model damps momentum in the model interior as a function of horizontal gradients (and a damping time scale τ), and a smaller domain size implies larger gradients, and thus more momentum diffusion. But larger horizontal gradients in SST, buoyancy (or α) and vorticity (Equations 3-2) also strengthen horizontal advection and the vorticity.

Figure 10a shows how convective tops change using a smaller domain (L = 500 km, black dot-dashed line) and a larger domain (L = 6000 km, black dashed line), while keeping τ unchanged. On the smaller ($L = 500$ km) domain deep convection collapses immediately to shallow convection. On the larger domain a congestus mode is maintained, and the shallow modes are also deeper.

The profiles of the buoyancy gradient (dT_v/dx), u and ω help us understand this behaviour (Figure 11, top and middle panels). The gradients of the $L = 500$ km run in this Figure ($1/dx$) have been scaled (reduced by a factor of six) to compare with the control run. Figure 11f thus shows that (after scaling) the gradients in T_v are relatively small for $L = 500$ km run compared to the control run (Figure 11a), especially above 900-850 hPa. Temperature gradients above those levels, for instance, those created by stronger evaporative or radiative cooling from congestus tops, are apparently difficult to maintain as buoyancy waves and damping become more effective at removing them. In other words, the weak virtual temperature gradient (WTG) approximation applies much better when using small domains.

Without scaling, the gradients in T_v in the boundary layer are much larger for the $L = 500$ km domain. Therefore, the shallow and congestus modes (in blue and green) have a stronger circulation, which is marked by a larger maximum in subsidence near the cold-side convective tops. The near-surface wind speed at the column boundary is nevertheless smaller, because the two-column system requires mass continuity:

$$u = -\int \left(\frac{d\omega}{dp}\right) dx \tag{9}$$

whereby a larger $d\omega/dp$ is easily outweighed by a six times smaller dx.

A more accurate approach would be to reduce the damping time scale τ (Table 1) along with reducing the domain size, although there is no clear theory at hand for how to do so. Using a six times smaller τ (not shown), the damping applied to the model interior is even stronger, yet the results are very similar. In this model, the influence of domain size is thus exerted mostly through the buoyancy gradients and advective tendencies, and less so through damping. However, the model applies other sources of momentum diffusion, which are more important for the development of congestus.

5.2.2 | Momentum diffusion through CMT and the PBL

One source of momentum diffusion is the transport of momentum by the buoyancy-sorted updrafts and downdrafts (convective momentum transport, CMT), which is represented by F_c^u in Equation 3. Additionally, turbulent mixing in the boundary layer produces a vertical diffusion of momentum, which in the model is represented through the term $\frac{\partial \nu(\partial \eta/\partial p)}{\partial p}$ in the same equations, whereby ν depends on the damping time scale ($\gamma \propto 1/\tau$) and the boundary layer depth (Δ_{PBL}). Both processes have a similar effect on the results: they damp buoyancy waves that tend to smooth virtual temperature gradients. In doing so, they allow buoyancy gradients between the columns to persist.

The importance of CMT for convective tops can be seen when contrasting the runs with CMT for different domain sizes (Figure 10a) with runs in which CMT is turned off (Figure 10b). For example, using the control domain size ($L = 3000$ km, solid line) the lower congestus modes near 650 hPa (in green) disappear in absence of CMT, and the deep and

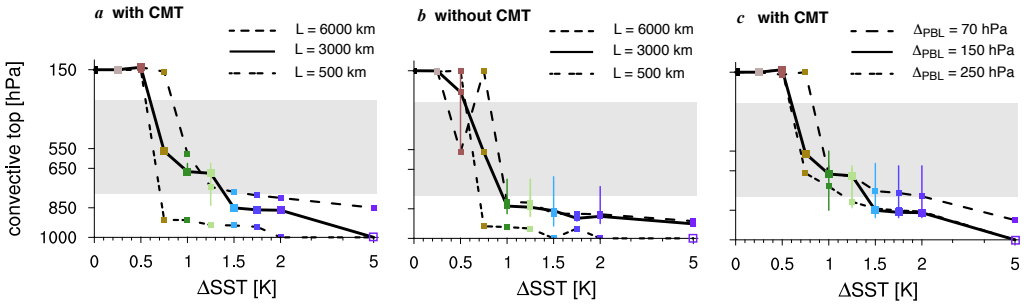

FIGURE 10 Convective tops over the cold ocean as a function of ΔSST as in Figure 6a), but here for different horizontal domain sizes in runs with CMT (a) and runs without CMT (b), and (c) for different PBL depths for momentum flux convergence, including Δ_{PBL} = 70 hPa, 150 hPa (control) and 250 hPa.

shallow modes are overall more unstable. The congestus mode near 550 hPa is not sensitive to CMT, and present in most parameter configurations.

The thermodynamic gradients and structure of the circulation for the 'no CMT' runs are shown in the bottom panels of Figure 11. These reveal that turning off CMT has a similar influence on the buoyancy gradient as using a smaller domain (L = 500 km): above the boundary layer (850 hPa), buoyancy gradients have disappeared (Figure 11k) compared to the control run (Figure 11a). Without CMT the runs using ΔSST = 1 and 1.75 K also develop stronger near-surface winds and larger peaks in subsidence (Figures 11n and o), as the cold-side inversion is getting stronger (Figure 11l).

The zonal wind component of the circulation that develops is solved at column boundaries, but in the two-column system only one boundary exists: that between the two columns. Hence, CMT might have a stronger influence on the circulation here than is realistic. Nevertheless, the runs illustrate that CMT might be relevant for the development of convection in circulations not strongly influenced by planetary rotation. Indeed, Kuang (2012) has demonstrated that the WTG assumption is too stringent for mock-Walker circulations, especially on large domains, which require larger temperature anomalies to drive the flow. Pronounced horizontal flows and the presence of more than one overturning cell have also been found in a CRM and mesoscale model (Posselt *et al.*, 2008; Pakula and Stephens, 2009). Moreover, Lin *et al.* (2008) show that CMT and non-linear advection contribute significantly to the damping that is required to balance pressure gradient forces in regions where the Coriolis force is small, and justify the strong Rayleigh damping applied in Matsuno-Gill type of models of tropical overturning circulations.

The WTG approximation does not apply within the boundary layer because of efficient momentum diffusion by turbulence. The depth of momentum diffusion (Δ_{PBL}) is 150 hPa in the control run. Because the convective tops of the shallow modes are near 850 hPa, Δ_{PBL} is suspected to play a role in setting these tops. But decreasing Δ_{PBL} to 70 hPa leads to the opposite behaviour of what one might expect: the tops of the shallow modes (blue), and even a congestus mode (yellow), are raised instead of lowered (dashed lines in Figure 10c).

An explanation for this behaviour lies in the strength of the circulation, which is ultimately forced by the buoyancy gradient between the two columns. The total integrated buoyancy gradient increases as the depth Δ_{PBL} over which gradients are maintained increases. If we simplify Equation 3 by considering an equilibrium state ($\frac{\partial \eta}{\partial t}$ = 0), ignoring advection, rotation and CMT, and assuming that the explicit damping is small compared to the momentum flux convergence in the boundary layer, a balance between the buoyancy gradient term and the momentum flux convergence must exist:

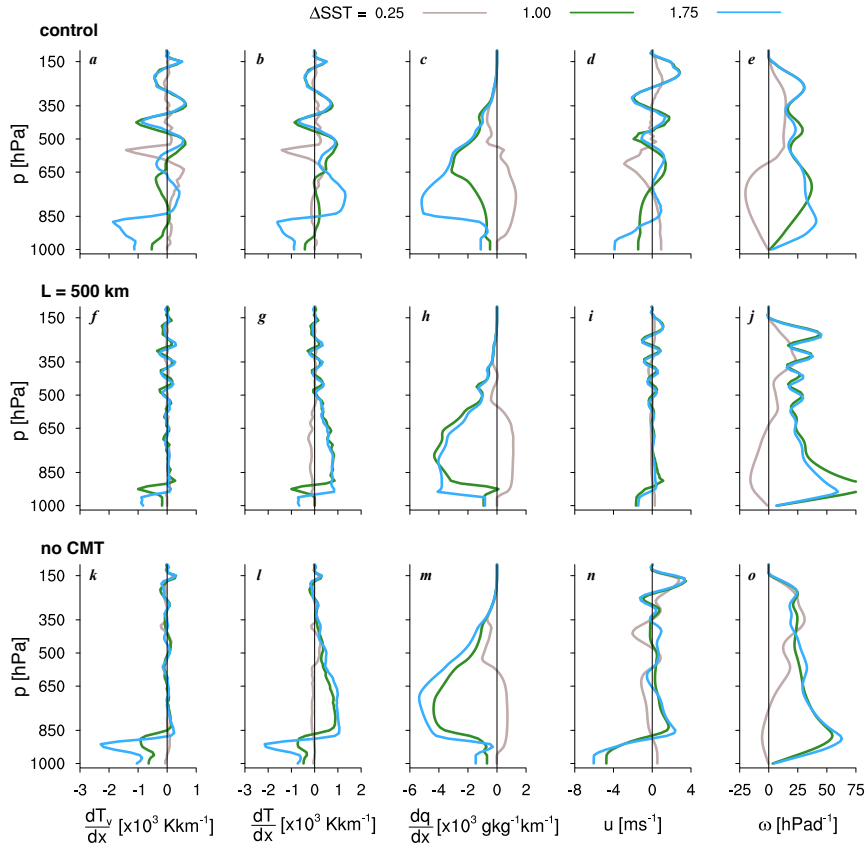

FIGURE 11 Profiles of the thermodynamic gradients and structure of the circulation over the cold SST column for the control run (top panels, similar to Figure 7), for a run with a smaller domain size of L =500 km (middle panels) and for a run in which CMT is turned off (bottom panels). For the L =500 km run, the gradients have been reduced by a factor of 6, corresponding to the reduction in domain size. Plotted are (from left to right): the virtual temperature (buoyancy) gradient between the two columns dT_v/dx; the temperature gradient dT/dx ; the specific humidity gradient dq/dx; the horizontal velocity u at the column boundary; and the vertical velocity over the cold ocean ω^{cold}.

$$0 = \frac{\partial \alpha}{\partial x} + \frac{\partial \nu(\partial \eta / \partial p)}{\partial p} \tag{10}$$

The viscosity ν vanishes above the boundary layer. Hence, if we integrate from the surface p_s up to the top of the boundary layer $p_s - \Delta_{\mathrm{PBL}}$, and rearrange the stress term to the left hand side, we can write:

$$\nu_s \left(\frac{\partial \eta}{\partial p} \right)_s = \int_{p_s}^{p_s - \Delta \mathrm{PBL}} \frac{\partial \alpha}{\partial x} dp \tag{11}$$

The left hand side represents a measure of the strength of the circulation, *e.g.* the strength of the divergence in horizontal wind near the surface. By lowering Δ_{PBL} to 70 hPa, the circulation will weaken. The strong temperature gradients that exist near 850 hPa (Figure 11a) also weaken (not shown), which leads to less low-level subsidence over the cold ocean. In turn, this allows the shallow mode to deepen to congestus. But in absence of momentum dissipation above $p_s - \Delta_{\mathrm{PBL}}$ any gradients introduced by the deeper convection are hard to maintain, which results in an oscillation between shallow and congestus tops (Figure 10c).

If we compare the sensitivity of the tops of the shallow mode to different perturbations in Figures 6 and 10 we may conclude that shallow tops are strongly regulated by the circulation as set by the buoyancy gradient (and thus domain size) and the ability to sustain such a gradient through momentum diffusion in the lower atmosphere. Namely, the shallow tops are fairly robust, because the circulation introduces a negative feedback: an increase in the depth of the diffusive layer with a deepening of convection and the boundary layer leads to a larger buoyancy contrast, and therefore, stronger subsidence over the cold ocean, which in turn limits the depth of the diffusive layer. Only when the buoyancy gradients are changed independently of the convection, by changing the domain size, is a significant change in the tops of the shallow mode observed (Figures 10a and b).

6 | CONCLUSIONS

Through time-integration of a two-column model with parameterized physics we have studied mechanisms that set the depth of convection in the subsiding branch of a Walker-like circulation. The circulations are achieved by prescribing a range of SST gradients between the columns. At a number of vertical resolutions, the model produces a trimodality in convective tops, similar to that in nature and in CRMs (Johnson *et al.*, 1999; Posselt *et al.*, 2008; Mechem and Oberthaler, 2013). With increasing SST gradient, convection over the cold ocean collapses from deep convection with tops near 150 hPa, to cumulus *congestus*, with tops near 550 hPa and near 650 hPa, and then to shallow cumulus, with tops near 850 hPa. The multiple modes of convection are a surprising feature of the model, because coarse-resolution models with parameterized convection generally produce a bimodal distribution of convective tops. Moreover, the convection scheme does not explicitly include melting or freezing processes, which have been hypothesized as important for creating the stable layers that halt congestus.

The trimodal character of the convection can already be seen in time integrations towards local RCE, in which the convection scheme preferably detrains moisture near cloud-base, between 600-550 hPa ($\approx$ 50-100 hPa below 0°C) and at the tropopause. The level of neutral buoyancy (LNB) fluctuates between mid- and high-levels. Why the scheme detrains moisture at mid-levels in the absence of any stable layers due to freezing or melting is not fully understood, but we find that it depends on the profile of radiative cooling. Only when the radiative cooling profile has larger cooling

below mid-levels than above mid-levels, is the LNB regularly located at mid-levels. We hypothesize that such a radiative cooling profile leads to mid-level LNB's because the upper atmosphere becomes relatively stable to rising parcels.

When mid-level detrainment is regular, it will imprint on the humidity and stability profiles that are established towards local RCE. The humidity profile is relatively dry above 550 hPa, because little detrainment takes place between mid- and high-levels. Just above 550 hPa the stability increases, due to evaporative cooling of detrained condensate and the interaction of radiation with the humidity gradient.

Upon lowering the SST by at least a degree, deep convection over the cold ocean immediately collapses to congestus with tops below the base of that dry layer. Subsequently, convection deepens again, unless radiation can interact with the moisture detrained near cumulus tops, which increases the stability at the base of the dry layer (Mapes and Zuidema, 1996). Because radiative cooling from moisture detrained by congestus creates a larger heating contrast with the warm column, subsidence also maximizes near the tops of congestus and in the cloud layer, as suggested before by Pakula and Stephens (2009) and Posselt *et al.* (2011). Even when in real atmospheres the dry layers have a different origin, such as from intrusions of midlatitude air (Yoneyama and Parsons, 1999), the results emphasize the importance of water vapor, as reviewed in recent literature (Mapes *et al.*, 2017; Stevens *et al.*, 2017), and its potential influence in setting convective tops not only through entrainment processes.

The congestus modes are very sensitive to model physics, and the lower congestus modes is only stable when enough momentum diffusion exists above the boundary layer, which allows buoyancy gradients, such as created through evaporative cooling near congestus tops, to persist against the work of buoyancy waves. In other words, momentum diffusion permits stronger temperature gradients. This is true on large domains, or when having ample convective momentum transport (CMT). Perhaps the sensitive nature of this congestus mode holds some relevance to the real world, where congestus is never observed to dominate the cloud field on the scale of a Hadley or Walker cell. For the Hadley cell, where planetary rotation prevents WTG, the relative importance of CMT is probably much smaller. But the importance of CMT might be relevant for the Walker circulation (Lin *et al.*, 2008; Kuang, 2012), or for circulations on smaller scales, where cumulus congestus is frequently observed near the leading edges of organised convective systems.

Despite the clear limitations of this modelling framework, the results suggest some ideas to be explored in future studies. First, they suggest the potential importance of an interaction between momentum (dynamics) and thermodynamics (convection) through momentum diffusion by turbulence and convection. Furthermore, they suggest that deep convection, by setting the structure of the humidity profile, can influence the vertical extent of nearby shallower convection. In future work, we will address the origin of congestus in overturning circulations by running a doubly periodic CRM with an idealised SST gradient in one direction, following setups such as used in Bretherton *et al.* (2006) and Nolan *et al.* (2010), or by coupling two CRM columns using the WTG approximation (Daleu *et al.*, 2012).

ACKNOWLEDGEMENTS

The first author would like to thank the EAPS department at MIT for hosting her as a postdoctoral fellow, and the Max Kade Foundation, the Max Planck Society, and Professors Reimar Lüst, Bjorn Stevens and Martin Claussen for their funding and support. Professor Chris Bretherton and Dr. Cathy Hohenegger are thanked for insightful discussions. The second author was supported by the National Science Foundation under grant AGS-1418508. We greatly appreciate the insightful comments by two critical reviewers.

REFERENCES

Bellon G, Treut HL. 2003. Large-scale and evaporation-wind feedbacks in a box model of the tropical climate. *Geophysical Research Letters* **30**(22): 2145.

Bony S, Emanuel KA. 2001. A Parameterization of the Cloudiness Associated with Cumulus Convection ; Evaluation Using TOGA COARE Data. *J. Atmos. S* **58**: 3158–3183.

Bretherton CS, Blossey PN, Peters ME. 2006. Interpretation of simple and cloud resolving simulations of moist convection radiation interaction with a mock Walker circulation. *Theoretical and Computational Fluid Dynamics* **20**(5): 421–442.

Bretherton CS, Sobel AH. 2002a. A simple model of a convectively coupled walker circulation using the weak temperature gradient approximation. *Journal of Climate* **15**(20): 2907–2920.

Bretherton CS, Sobel AH. 2002b. A simple model of a convectively coupled walker circulation using the weak temperature gradient approximation. *Journal of Climate* **15**(20): 2907–2920.

Clement A, Seager R. 1999. Climate and the tropical oceans. *Journal of Climate* **12**(12): 3383–3401.

Daleu CL, Woolnough SJ, Plant RS. 2012. Cloud-Resolving Model Simulations with One- and Two-Way Couplings via the Weak Temperature Gradient Approximation. *Journal of the Atmospheric Sciences* **69**(12): 3683–3699.

Emanuel K. 2007. Quasi-equilibrium dynamics of the tropical atmosphere. In: *The Global Circulation of the Atmosphere*, Schneider T, Sobel AH (eds), ch. 7, Princeton University Press, p. 385pp.

Emanuel KA. 1991. A Scheme for Representing Cumulus Convection in Large-Scale Models. *Journal of the Atmospheric Sciences* **48**(21): 2313–2329.

Emanuel KA, Zivkovic-Rothman M. 1999. Development and Evaluation of a Convection Scheme for Use in Climate Models. *J. Atmos. Sci* **56**: 1766–1782.

Fouquart Y, Bonnell B. 1980. Computation of solar heating of the Earth's atmosphere: A new parameterization. *Contrib. Atmos. Phys.* **53**: 35–62.

Hohenegger C, Stevens B. 2016. Coupled radiative convective equilibrium simulations with explicit and parameterized convection. *Journal of Advances in Modeling Earth Systems* **8**(3): 1468–1482.

Inness PM, Slingo JM, Woolnough SJ, Neale RB, Pope VD. 2001. Organization of tropical convection in a GCM with varying vertical resolution; implications for the simulation of the Madden Julian Oscillation. *Climate Dynamics* **17**(10): 777–793.

Jensen MP, Genio ADD. 2006. Factors Limiting Convective Cloud-Top Height at the ARM Nauru Island Climate Research Facility. *Journal of Climate* **19**(10): 2105–2117.

Johnson RH, Rickenbach TM, Rutledge SA, Ciesielski PE, Schubert WH. 1999. Trimodal Characteristics of Tropical Convection. *Journal of Climate* **12**(8): 2397–2418.

Kuang Z. 2012. Weakly Forced Mock Walker Cells. *Journal of the Atmospheric Sciences* **69**(9): 2759–2786.

Larson K, Hartmann DL, Klein SA. 1999. The role of clouds, water vapor, circulation, and boundary layer structure in the sensitivity of the tropical climate. *Journal of Climate* **12**(8 PART 1): 2359–2374.

Lin JL, Mapes BE, Han W. 2008. What Are the Sources of Mechanical Damping in Matsuno Gill Type Models? *Journal of Climate* **21**(2): 165–179.

Luo Z, Liu GY, Stephens GL, Johnson RH. 2009. Terminal versus transient cumulus congestus: A CloudSat perspective. *Geophysical Research Letters* **36**(5): 4–7.

562 Mapes B, Chandra AS, Kuang Z, Zuidema P. 2017. Importance Profiles for Water Vapor. *Surveys in Geophysics* **38**(6): 1355–
563 1369.

564 Mapes BE, Houze Ra. 1995. Diabatic divergence profiles in western Pacific mesoscale convective systems. *Journal of the Atmo-*
565 *spheric Sciences* **52**(10): 1807–1828.

566 Mapes BE, Zuidema P. 1996. Radiative-Dynamical Consequences of Dry Tongues in the Tropical Troposphere. *Journal of the*
567 *Atmospheric Sciences* **53**(4): 620–638.

568 Mauritsen T, Stevens B. 2015. Missing iris effect as a possible cause of muted hydrological change and high climate sensitivity
569 in models. *Nature Geosci* **8**(5): 346–351.

570 Mechem DB, Oberthaler aJ. 2013. Numerical simulation of tropical cumulus congestus during TOGA COARE. *Journal of Ad-*
571 *vances in Modeling Earth Systems* **5**(July): n/a–n/a.

572 Miller RL. 1997. Tropical thermostats and low cloud cover. *Journal of Climate* **10**(3): 409–440.

573 Morcrette JJ. 1991. Radiation and cloud radiative properties in the European Centre for Medium Range Weather Forecasts
574 forecasting system. *Journal of Geophysical Research: Atmospheres* **96**(D5): 9121–9132.

575 Muller CJ, Held IM. 2012. Detailed Investigation of the Self-Aggregation of Convection in Cloud-Resolving Simulations. *Journal*
576 *of the Atmospheric Sciences* **69**(8): 2551–2565.

577 Naumann AK, Stevens B, Hohenegger C, Mellado JP. 2017. A Conceptual Model of a Shallow Circulation Induced by Prescribed
578 Low-Level Radiative Cooling. *Journal of the Atmospheric Sciences* **74**(10): 3129–3144.

579 Neggers RAJ, Neelin JD, Stevens B. 2007. Impact Mechanisms of Shallow Cumulus Convection on Tropical Climate Dynamics*.
580 *Journal of Climate* **20**(11): 2623–2642.

581 Nilsson J, Emanuel K. 1999. Equilibrium atmospheres of a two-column radiative-convective model. *Quarterly Journal of the*
582 *Royal Meteorological Society* **125**: 2239–2264.

583 Nolan DS, Powell SW, Zhang C, Mapes BE. 2010. Idealized Simulations of the Intertropical Convergence Zone and Its Multi-
584 level Flows. *Journal of the Atmospheric Sciences* **67**(12): 4028–4053.

585 Nuijens L, Medeiros B, Sandu I, Ahlgrimm M. 2015. Observed and modeled patterns of covariability between low-level cloudi-
586 ness and the structure of the trade-wind layer. *Journal of Advances in Modeling Earth Systems* **7**(4): 1741–1764.

587 Pakula L, Stephens GL. 2009. The Role of Radiation in Influencing Tropical Cloud Distributions in a Radiative Convective Equi-
588 librium Cloud Resolving Model. *Journal of the Atmospheric Sciences* **66**(1): 62–76.

589 Pauluis O, Emanuel K. 2004. Numerical Instability Resulting from Infrequent Calculation of Radiative Heating. *Monthly*
590 *Weather Review* **132**(3): 673–686.

591 Peters ME, Bretherton CS. 2005. A simplified model of the Walker circulation with an interactive ocean mixed layer and cloud-
592 radiative feedbacks. *Journal of Climate* **18**(20): 4216–4234.

593 Pierrehumbert RT. 1995. Thermostats, Radiator Fins, and the Local Runaway Greenhouse. *Journal of the Atmospheric Sciences*
594 **52**(10): 1784–1806.

595 Posselt DJ, van den Heever S, Stephens G, Igel MR. 2011. Changes in the Interaction between Tropical Convection, Radiation,
596 and the Large-Scale Circulation in a Warming Environment. *Journal of Climate* **25**(2): 557–571.

597 Posselt DJ, van den Heever SC, Stephens GL. 2008. Trimodal cloudiness and tropical stable layers in simulations of radiative
598 convective equilibrium. *Geophysical Research Letters* **35**(8): L08 802.

Raymond DJ, Blyth AM. 1986. A Stochastic Mixing Model for Nonprecipitating Cumulus Clouds. *Journal of the Atmospheric Sciences* **43**(22): 2708–2718.

Riehl H, Yeh TC, Malkus JS, la Seur NE. 1951. The north-east trade of the Pacific Ocean. *Quarterly Journal of the Royal Meteorological Society* **77**(334): 598–626.

Sherwood SC, Bony S, Dufresne JL. 2014. Spread in model climate sensitivity traced to atmospheric convective mixing. *Nature* **505**(7481): 37–42.

Stevens B, Brogniez H, Kiemle C, Lacour JL, Crevoisier C, Kiliani J. 2017. Structure and Dynamical Influence of Water Vapor in the Lower Tropical Troposphere. *Surveys in Geophysics* doi:10.1007/s10712-017-9420-8.

Sun DZ, Liu Z. 1996. Dynamic Ocean-Atmosphere Coupling : A Thermostat for the Tropics. *Science* **272**(5265): 1148–1150.

Tiedtke M. 1989. A comprehensive mass flux scheme for cumulus parameterization in large-scale models. *Monthly Weather Review* **117**: 1779–1800.

Vial J, Bony S, Dufresne JL, Roehrig R. 2016. Coupling between lower-tropospheric convective mixing and low-level clouds: Physical mechanisms and dependence on convection scheme. *Journal of Advances in Modeling Earth Systems* **8**(4): 1892–1911.

Wing AA, Emanuel KA. 2014. Physical mechanisms controlling self-aggregation of convection in idealized numerical modeling simulations. *Journal of Advances in Modeling Earth Systems* **6**(1): 59–74.

Yoneyama K, Parsons DB. 1999. A Proposed Mechanism for the Intrusion of Dry Air into the Tropical Western Pacific Region. *Journal of the Atmospheric Sciences* **56**(11): 1524–1546.

Zhang C, Nolan DS, Thorncroft CD, Nguyen H. 2008. Shallow meridional circulations in the tropical atmosphere. *Journal of Climate* **21**(14): 3453–3470.